



## ISTITUTO NAZIONALE DI RICERCA METROLOGICA Repository Istituzionale

Cation distribution effect on static and dynamic magnetic properties of  $\text{Co}_{1-x}\text{Zn}_x\text{Fe}_2\text{O}_4$  ferrite powders

This is the author's submitted version of the contribution published as:

*Original*

Cation distribution effect on static and dynamic magnetic properties of  $\text{Co}_{1-x}\text{Zn}_x\text{Fe}_2\text{O}_4$  ferrite powders / Barrera, G.; Coisson, M.; Celegato, F.; Raghuvanshi, S.; Mazaleyrat, F.; Kane, S. N.; Tiberto, P.. - In: JOURNAL OF MAGNETISM AND MAGNETIC MATERIALS. - ISSN 0304-8853. - 456:(2018), pp. 372-380. [10.1016/j.jmmm.2018.02.072]

*Availability:*

This version is available at: 11696/65800 since: 2021-01-28T16:38:10Z

*Publisher:*

Elsevier

*Published*

DOI:10.1016/j.jmmm.2018.02.072

*Terms of use:*

This article is made available under terms and conditions as specified in the corresponding bibliographic description in the repository

*Publisher copyright*

(Article begins on next page)

# Cation distribution effect on static and dynamic magnetic properties of $\text{Co}_{1-x}\text{Zn}_x\text{Fe}_2\text{O}_4$ ferrite powders

G. Barrera<sup>a,\*</sup>, M. Coisson<sup>a</sup>, F. Celegato<sup>a</sup>, S. Raghuvanshi<sup>b</sup>, F. Mazaleyrat<sup>c</sup>, S. N. Kane<sup>b</sup>, P. Tiberto<sup>a</sup>

<sup>a</sup>INRiM, Nanoscience and Materials Division, Strada delle Cacce 91, I-10135 Torino, Italy

<sup>b</sup>School of Physics, Devi Ahilya University, Khandwa road Campus, Indore-452001, India

<sup>c</sup>SATIE, ENS de Cachan, CNRS 8029, Universite Paris-Saclay, 61 Av. President Wilson, 94235 Cachan, France

\*Corresponding author at: National Institute of Metrological Research (INRiM), Strada delle Cacce 91, I-10135 Torino, Italy. E-mail address: [g.barrera@inrim.it](mailto:g.barrera@inrim.it)

## Abstract

$\text{Co}_{1-x}\text{Zn}_x\text{Fe}_2\text{O}_4$  ( $0.08 \leq x \leq 0.56$ ) powders prepared by a sol gel auto-combustion method have been investigated through the combined use of structural and dc/ac-magnetization measurements under a wide range of applied magnetic field values. EDS spectra are performed to evaluate the samples chemical composition, whereas the X-ray diffraction measurements indicate the formation of the typical nanocrystalline mixed cubic spinel structure and allow to determine the cationic distribution as well as the lattice parameter and the oxygen position as function of Zn content. Magnetic characterization improves the knowledge about the correlation between the structural properties and magnetic behavior. The magnetization curves show a hysteretic behavior at room temperature and they are analyzed as function of Zn content taking in account the Yafet-Kittel's model. The replacement of non-zero magnetic moment  $\text{Co}^{2+}$  ions with zero magnetic moment  $\text{Zn}^{2+}$  ions induces a gradual reduction of magnetocrystalline anisotropy and a lowering of the magnetic coercivity. The energy lost in a static and alternating magnetic field (frequency of 69 kHz) at selected vertex field values for the studied samples has been calculated in order to evaluate their prospective usage to operate in different field conditions.

## Keywords

Cobalt-Zinc ferrites; non-equilibrium cation distribution; structure characterization; magnetic characterization; energy losses.

# 1. Introduction

Ceramic spinel ferrite particles exhibit different peculiar properties e.g. high electrical resistivity, low-power loss at high frequency, high magnetic saturation and coercivity [1–4]. These properties make ferrites a viable alternative to replace rare-earth elements in permanent magnets [5] as well as suitable materials for various applications especially operating at high frequency [6–8].

Moreover, the large fraction of empty interstitial sites in the spinel ferrites face-centered cubic (fcc) structure encourages their filling with suitable divalent cations allowing one to finely tune the ferromagnetic behavior of ferrites according to practical demands [9].

X-ray diffraction (XRD) [10], neutron diffraction (ND) [11], extended x-ray absorption fine structure (EXAFS) [12] and Mössbauer spectroscopy (MS) [13] are usually used to obtain sensible information on cation distribution in the fcc structure. ND and EXAFS provide accurate analysis but require the access to neutron and synchrotron sources, respectively, increasing the cost and limiting the achievement of quick results. Also MS is a powerful tool to study environment around Fe atom, however it loses its power when non-magnetic ions are in focus. These limitations have created a need for the use of a relatively simpler but equally accurate method to obtain reliable results. In this context, XRD has established as one of the most suitable and successful tools for proper determination of cation distribution [10,14,15], although the effectiveness of XRD is partially limited by the similar scattering factors of some of the cations present in the spinel structure.

Commonly, the cation distribution of ferrites is influenced by different factors such as the preparation method, the stoichiometry and the condition of post-preparation heat treatments ending in many cases with a non-equilibrium cation distribution [16]. A fine tuning of this non-equilibrium structure is a powerful tool for tailoring the magnetic properties of ferrites. In general, non-equilibrium distribution is expected in dry gel samples synthesized at relatively low temperature where the cations do not have sufficient energy to reach their equilibrium occupancy [17,18].

$\text{Co}_{1-x}\text{Zn}_x\text{Fe}_2\text{O}_4$  ferrites synthesized by various techniques have been extensively reported in literature revealing how their structural and magnetic properties (e.g. lattice parameter, saturation magnetization, coercivity, blocking temperature and magnetic anisotropy) can be controlled with a fine tune of Zn cation content inducing a desired cation distribution [19–22].

In the present study,  $\text{Co}_{1-x}\text{Zn}_x\text{Fe}_2\text{O}_4$  ( $0.08 \leq x \leq 0.56$ ) are synthesized in ‘dry gel’ form by exploiting sol gel auto-combustion method. XRD characterization is successfully used to determine information on their structural properties and to calculate the cation distribution. Magnetic characterization is performed with an aim to improve the knowledge about the correlation between structural properties and the magnetic behavior as function of Zn content. In addition, energy dissipated by the samples submitted to selected values of static and dynamic magnetic fields are also evaluated.

## 2. Experimental

$\text{Co}_{1-x}\text{Zn}_x\text{Fe}_2\text{O}_4$  powder samples were prepared by sol-gel auto-combustion method utilizing citrate-nitrate precursors at low temperature ( $< 110^\circ\text{C}$ ) without any post-preparation heat treatments as described earlier [23,24]. The selected nominal Zn concentration was  $x = 0.08, 0.16, 0.24, 0.32, 0.40, 0.48, 0.56$ .

X-ray diffraction (XRD) patterns of the synthesized samples were recorded in  $\theta$ - $2\theta$  configuration with Bruker D8 advance diffractometer utilizing  $\text{CuK}\alpha$  radiation, equipped with fast counting detector based on silicon strip technology Bruker LynxEye detector; XRD data was analyzed to obtain structural parameters and the cation distribution of samples [25]. As Co and Zn have rather different scattering factors, the determination of their distribution using XRD technique was reliable.

The morphology of obtained powder samples was observed by means of scanning electron microscopy (SEM, FEI Inspect-F). The SEM electron beam was also used to recover elemental spectra collecting the characteristic X-ray lines of the elements of interest through Energy Dispersive Spectroscopy (EDS) detector in order to confirm the Zn concentration. K and L lines of elements were detected using an accelerating voltage of 30 kV and a beam dwell time of 300 s.

Room-temperature static (dc) magnetization curves were measured by means of an alternating gradient field magnetometer (AGFM). The samples suitable for AGFM measurements were prepared by mixing a known mass of  $\text{Co}_{1-x}\text{Zn}_x\text{Fe}_2\text{O}_4$  powder with wax, forming a solid pellet. The dc-hysteresis loops were measured both at the maximum magnetic field that the AGFM can apply (18 kOe) and at selected vertex fields in the range 100 - 1000 Oe.

Saturation magnetization values at 2 K were measured on all samples by means of a SQUID magnetometer by applying a magnetic field of 70 kOe.

Dynamic (ac) hysteresis loops were performed on all samples by means of a custom-built B-H loop tracer [26] generating an alternating magnetic field with a frequency of ~69 kHz and amplitude in the range 100 – 525 Oe; ac-loops were measured at selected vertex fields in the allowable range.

### 3. Results and discussion

#### 3.1 Structural properties

The x-ray diffraction (XRD) patterns of  $\text{Co}_{1-x}\text{Zn}_x\text{Fe}_2\text{O}_4$  ( $0.08 \leq x \leq 0.56$ ) spinel ferrite powders are presented in Fig. 1a. Rietveld refinement done by using Material Analysis Using Diffraction (MAUD) software [27] for  $\text{Co}_{0.52}\text{Zn}_{0.48}\text{Fe}_2\text{O}_4$  composition is illustrated in Fig. 1b; it is representative of all samples. XRD peaks confirm the formation of single phase nanocrystalline mixed cubic spinel structure (space group  $Fd\bar{3}m$ ) independently of the Zn content (x).

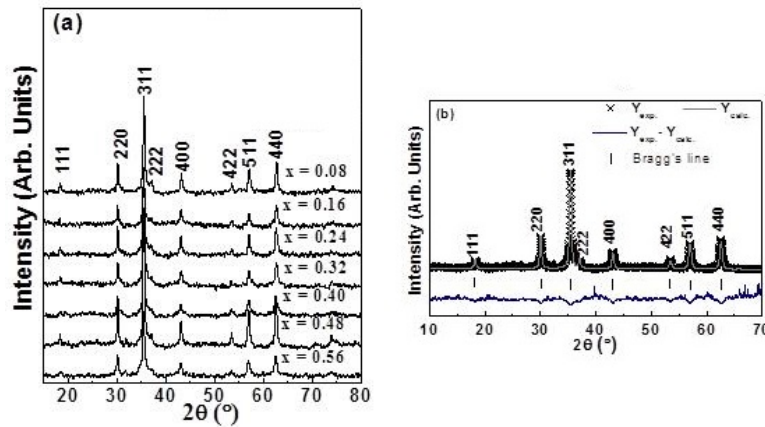


**Figure 1:** (a) XRD patterns of  $\text{Co}_{1-x}\text{Zn}_x\text{Fe}_2\text{O}_4$  samples ( $0.08 \leq x \leq 0.56$ ). (b) Rietveld refined XRD of  $\text{Co}_{0.52}\text{Zn}_{0.48}\text{Fe}_2\text{O}_4$  sample.

The morphology of  $\text{Co}_{0.44}\text{Zn}_{0.56}\text{Fe}_2\text{O}_4$  and  $\text{Co}_{0.52}\text{Zn}_{0.48}\text{Fe}_2\text{O}_4$  ferrite powder samples is shown in Fig. 2 (panel a and b, respectively); the micrographs shown are representative of all samples. A quite complex grain arrangement is observed in both compositions, constituted by a micrometric structure or agglomerate with a surface similar to a beehive, composed by nano-sized crystals. These characteristics are due to the sol-gel

auto-combustion synthesis process in which a lot of gases are liberated from gels during the drying process following the combustion [28]. Similar morphology composed by micrometric polycrystalline agglomerates has been already observed in ferrite powders prepared with comparable auto-combustion methods [28–31].

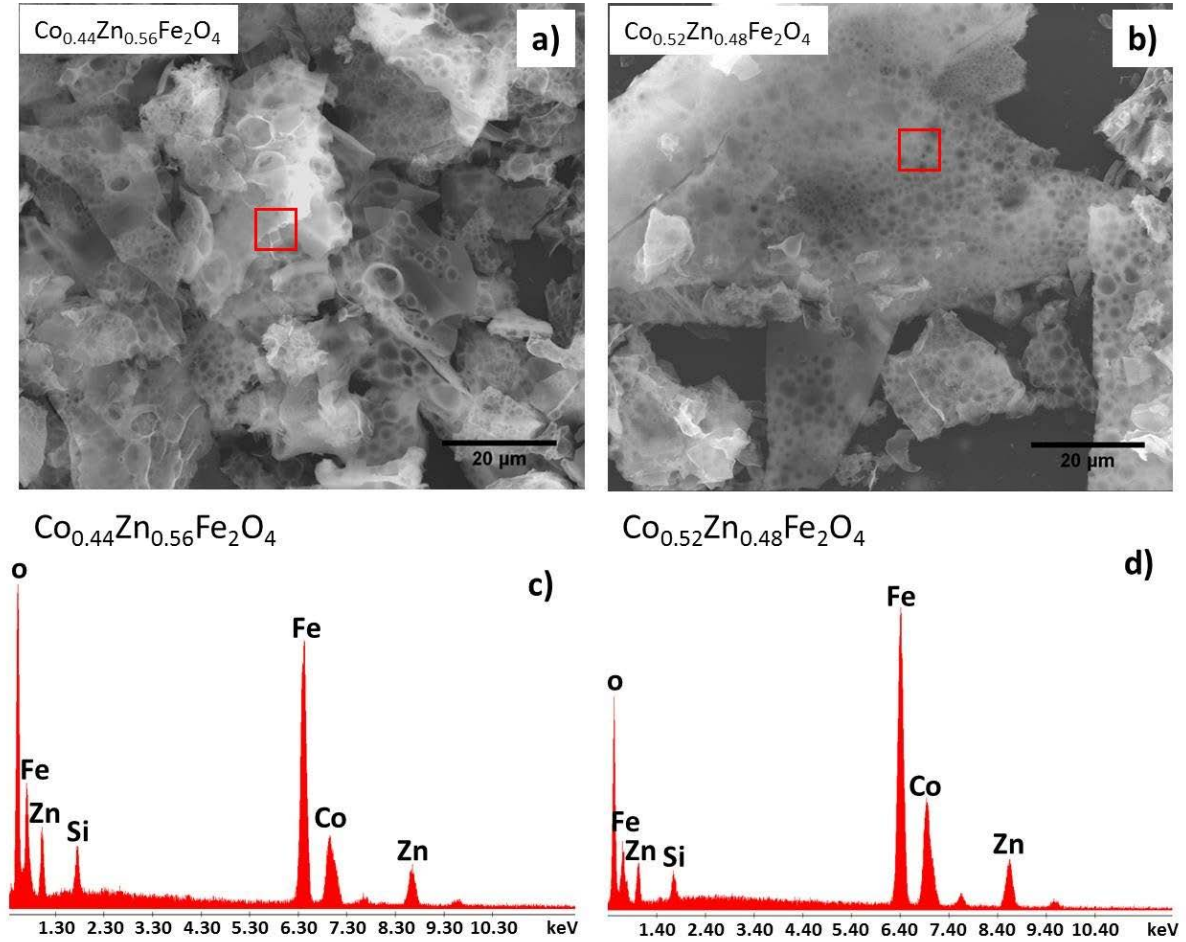


**Figure 2:** Morphology of the  $\text{Co}_{0.44}\text{Zn}_{0.56}\text{Fe}_2\text{O}_4$  (panel a) and  $\text{Co}_{0.52}\text{Zn}_{0.48}\text{Fe}_2\text{O}_4$  (panel b) ferrite powder samples; EDS spectra of the  $\text{Co}_{0.44}\text{Zn}_{0.56}\text{Fe}_2\text{O}_4$  (panel c) and  $\text{Co}_{0.52}\text{Zn}_{0.48}\text{Fe}_2\text{O}_4$  (panel d) ferrite powder samples. The red squares in the SEM images (panel a and b) represent the analyzed area to obtain the EDS spectra.

In order to obtain information about the micrometric agglomerates of ferrite powders observed in SEM images (Fig. 2 panel a and b), the grain mean diameter  $\langle D_{XRD} \rangle$  was calculated from XRD data with Scherrer's equation for all samples. The  $\langle D_{XRD} \rangle$  values are given in the table 1 and they range between 23 and 35 nm indicating the formation of nano-crystallites within the observed agglomerates. Moreover, the tendency of  $\langle D_{XRD} \rangle$  values is to decrease with increasing Zn content (x) as already observed in similar structures [19,32,33].

Nominal Zn content (x)	$\langle D_{XRD} \rangle$ (nm)	EDS Zn content (x)
0.08	32.4	0.08(1)
0.16	34.9	0.17(1)
0.24	31.7	0.23(6)
0.32	24.5	0.33(6)
0.40	25.3	0.40(5)
0.48	28.6	0.46(4)
0.56	22.9	0.55(2)

**Table1:** Grain mean diameter,  $\langle D_{XRD} \rangle$  as a function of nominal Zn content (x) and comparison between nominal and measured (EDS) Zn content (x).

The EDS spectra of  $\text{Co}_{0.44}\text{Zn}_{0.56}\text{Fe}_2\text{O}_4$  and  $\text{Co}_{0.52}\text{Zn}_{0.48}\text{Fe}_2\text{O}_4$  samples are shown in Fig. 2 panel c and d, respectively; they are representative of all other compositions. The EDS signal is collected in a square area of the sample with size  $(7 \times 7) \mu\text{m}^2$  averaging on different nano-crystallites; red squares are added in SEM images in Fig. 2 panel a and b to identify the analyzed areas. In both spectra the peaks are clearly visible corresponding to the elements constituting the ferrite, i.e. Zn, Co, Fe and O; the peak of Si comes from the substrate on which the powder sample has been dispersed to perform the measurements. The atomic percentage (at.%) of elements calculated from EDS spectra allows to calculate the composition of samples. The calculated EDS Zn content (x) of each sample is reported in table 1. In the EDS analysis, only the Co and Zn contributions are taken into account, therefore only their relative amount is meaningful. As clearly reported in table 1, the Co/Zn relative amount as determined by EDS is in very good agreement with the nominal value.

The XRD data (Fig. 1a) are also analysed to obtain cation distribution in the studied samples via the Bertaut method [25]. In general, cation distribution of ferrites can be indicated as  $(\text{Me}_{\delta}^{\text{II}} \text{Fe}_{1-\delta}^{\text{III}})[\text{Me}_{1-\delta}^{\text{II}} \text{Fe}_{1+\delta}^{\text{III}}]\text{O}_4$ , ( $\text{Me}_{\delta}^{\text{II}} = \text{Zn}^{2+}, \text{Co}^{2+}$ ), where the ions on tetrahedral sites (sites A) are given in parentheses and the ions on octahedral sites (sites B) between the square brackets. The quantity  $\delta$  is a parameter correlated to the inversion degree ( $i = 1-\delta$ ): for a completely random distribution  $\delta = 1/3$ , for a normal spinel  $\delta = 1$  and for an inverse spinel  $\delta = 0$  [34].

The cation distribution of metal ions over the A and B sites and the consequent parameter  $\delta$  are influenced by some factors such as the electronic configurations of metal cations, their radius and

electrostatic energy [34].  $\text{CoFe}_2\text{O}_4$  ferrite shows a predominantly inverse structure with  $\text{Co}^{2+}$  ions mainly on B (octahedral) sites, whereas  $\text{ZnFe}_2\text{O}_4$  is found to be a normal spinel with  $\text{Zn}^{2+}$  ions generally on A (tetrahedral) sites [33]. Instead, Fe ions prefer equally both A and B sites of the spinel structure [33]. In addition, the cation distribution depends strongly also from the method of ferrites synthesis; for instance, in case of quenching from high temperature, different cation distribution could be obtained depending on the interplay between the diffusion rate of metal ions in the structure and the cooling rate [35]. The cation distribution calculated for all samples is collected in Table 2 and shows a predominant presence of  $\text{Zn}^{2+}$  ions on B site. These deviations with respect to the general preference of  $\text{Zn}^{2+}$  ions to occupy the tetrahedral (A) site clearly demonstrates the presence of non-equilibrium cation distribution in the samples to be ascribed to the sol-gel auto-combustion method at low temperature ( $< 110^\circ\text{C}$ ) and to the lack of a post-synthesis heat treatment which would improve the diffusion rate of metal ions in the structure towards a distribution closer to the equilibrium. Instead, for the  $\text{Co}^{2+}$  ions distribution, at low Zn content ( $x \leq 0.32$ ) the whole content of  $\text{Co}^{2+}$  ions is located on B site, in accordance with the usual situation. However, with the rise of Zn content ( $x \geq 0.40$ ) the increased amount of  $\text{Zn}^{2+}$  ions on B site forces a partial migration of  $\text{Co}^{2+}$  ions towards A site. In a similar way but with inverse direction (from A to B site), the higher Zn content ( $x$ ) forces also some  $\text{Fe}^{3+}$  ions to migrate.

The parameter  $\delta$  calculated from the cation distribution (shown in Table 2) starts with a completely inverse spinel structure ( $\delta = 0$ ) for the sample  $\text{Co}_{0.92}\text{Zn}_{0.08}\text{Fe}_2\text{O}_4$  and progressively increases with increasing  $\text{Zn}^{2+}$  content ending up to a totally random distribution ( $\delta = 0.33$ ) for the sample  $\text{Co}_{0.44}\text{Zn}_{0.56}\text{Fe}_2\text{O}_4$ .

Nominal Zn content (x)	Cation Distribution	Inversi on degree ( $\delta$ )	$a$ (nm)	$u$
0.08	$(\text{Co}_{0.00}\text{Zn}_{0.00}\text{Fe}_{1.00})[\text{Co}_{0.92}\text{Zn}_{0.08}\text{Fe}_{1.00}]\text{O}_4$	0	0.8379	0.3788
0.16	$(\text{Co}_{0.00}\text{Zn}_{0.05}\text{Fe}_{0.95})[\text{Co}_{0.84}\text{Zn}_{0.11}\text{Fe}_{1.05}]\text{O}_4$	0.05	0.8390	0.3791
0.24	$(\text{Co}_{0.00}\text{Zn}_{0.10}\text{Fe}_{0.90})[\text{Co}_{0.76}\text{Zn}_{0.14}\text{Fe}_{1.10}]\text{O}_4$	0.10	0.8391	0.3794
0.32	$(\text{Co}_{0.00}\text{Zn}_{0.11}\text{Fe}_{0.89})[\text{Co}_{0.68}\text{Zn}_{0.21}\text{Fe}_{1.11}]\text{O}_4$	0.11	0.8396	0.3794
0.40	$(\text{Co}_{0.04}\text{Zn}_{0.11}\text{Fe}_{0.85})[\text{Co}_{0.56}\text{Zn}_{0.29}\text{Fe}_{1.15}]\text{O}_4$	0.15	0.8401	0.3796
0.48	$(\text{Co}_{0.19}\text{Zn}_{0.10}\text{Fe}_{0.71})[\text{Co}_{0.33}\text{Zn}_{0.38}\text{Fe}_{1.29}]\text{O}_4$	0.29	0.8393	0.3806
0.56	$(\text{Co}_{0.29}\text{Zn}_{0.04}\text{Fe}_{0.67})[\text{Co}_{0.15}\text{Zn}_{0.52}\text{Fe}_{1.33}]\text{O}_4$	0.33	0.8398	0.3807

**Table 2:** Cation distribution calculated for all samples; inversion degree ( $\delta$ ) values; lattice parameter ( $a$ ); oxygen parameter ( $u$ ).



The lattice parameter ( $a$ ), obtained by XRD data analysis, is found to increase with increasing Zn content until  $x \leq 0.40$  as revealed by the values collected in Table 2. This trend can be attributed to partial replacement of an ion with lower ionic radius (ionic radius of  $\text{Co}^{2+}$ : 0.058 nm) with an ion whose ionic radius is slightly higher (ionic radius of  $\text{Zn}^{2+}$ : 0.060 nm). This also confirms that Zn is going into the spinel structure. As expected, the  $a$  values lie within the range of the lattice constants of extreme Zn concentrations (0.8369 nm for  $\text{CoFe}_2\text{O}_4$  and 0.8430 nm for  $\text{ZnFe}_2\text{O}_4$  [36]); however, they do not meet exactly the linear relation between the increase of crystal lattice constant and the increase of Zn concentration as predicted by Vegard's law [37]. This slight discrepancy from linear relation can be ascribed to the non-equilibrium cation distribution in our samples.

In the ideal ferrite structure, the oxygen ions form an fcc lattice with the cubic edge equal to  $1/2a$  and, in this ideal case, the oxygen parameter ( $u$ ) corresponds to  $u_{id} = 3/8$  [34]. This assertion is valid only in first approximation, as in the real case the tetrahedral sites (sites A) are too small to contain a metal ion which therefore would cause slight lattice distortions and a displacement of the four oxygen atoms. In this case, the oxygen parameter increases ( $u > u_{id}$ ) and it could be used as a quantitative measurement of oxygen displacement. In our samples, the oxygen parameter  $u$  was calculated from the analysis of X-ray powder diffraction data and the values are collected in Table 2; it lies in the range 0.3788 – 0.3807 and, as expected, it is slightly higher than  $u_{id}$  (3/8) due to the distortion induced by metal ions ( $\text{Co}^{2+}$  and  $\text{Zn}^{2+}$ ) contained in the tetrahedral site of the spinel structure. Therefore, the higher the concentration of metal ions on tetrahedral site (A), the larger is the displacement of oxygen anions. This statement is confirmed in Fig. 3, where the almost linear correlation between the oxygen parameter ( $u$ ) and the inversion parameter ( $\delta$ ), that represents the concentration of metal ions ( $\text{Co}^{2+}$  and  $\text{Zn}^{2+}$ ) in tetrahedral (A), is shown. As expected among the studied samples, the sample  $\text{Co}_{0.44}\text{Zn}_{0.56}\text{Fe}_2\text{O}_4$ , is characterized by highest inversion parameter value ( $\delta = 0.33$ , totally random spinel structure), and shows the highest lattice distortion and displacement of oxygen ions.

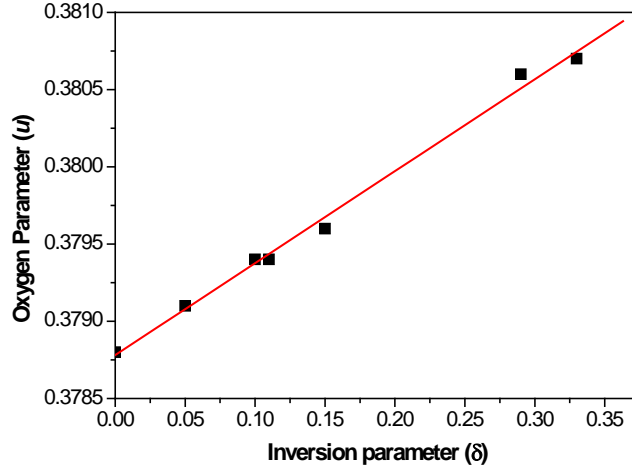


**Figure 3:** Oxygen parameter ( $u$ ) as a function of inversion parameter ( $\delta$ ); the red line is a guide to the eye.

In magnetic ferrites, it is worth noting that the strength of the magnetic interactions (A-O-B, B-O-B, and A-O-A) strongly depends on the inter-ionic separation between the cations, between the cation and the corresponding anion and on the bond angles between the cations [34]; in particular, the strength is inversely proportional to the bond length and it is highest when the bond angle is  $180^\circ$ . It is well known by comparing different exchange interactions that the A-O-B interaction is the strongest [34] and is responsible for the ferrimagnetic behavior exhibited by ferrites. Therefore, the inter-ionic lengths and bond angles on all the samples are evaluated in order to get information about the effect of  $\text{Zn}^{2+}$  and  $\text{Co}^{2+}$  ions on the strength of the magnetic interactions. In particular, the inter-ionic lengths between the cations ( $b$ ,  $c$ ,  $d$ ,  $e$  and  $f$ ), between the cation and anion ( $p$ ,  $q$ ,  $r$  and  $s$ ) and bond angles between the cations ( $\phi_1$ ,  $\phi_2$ ,  $\phi_3$ ,  $\phi_4$ ,  $\phi_5$ ) are calculated (not shown here) following the relations reported by Kumar et al. [38]. Regarding the strongest interaction A-O-B, the involved cation and anion length ( $p$  and  $q$  for length B-O and A-O, respectively) and the bond angles between the cations ( $\phi_1$ ) are shown in Fig. 4 as function of Zn (x) content.

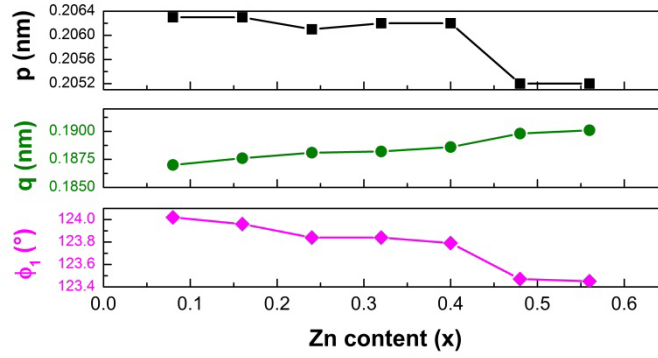


**Figure 4:** Inter-ionic lengths between the cation and anion ( $p$  and  $q$  for length B-O and A-O, respectively) and the bond angles between the cations ( $\phi_l$ ) as a function of Zn content ( $x$ ).

As function of Zn content ( $x$ ), a non-monotonic trend is found for the bond length  $p$ , being almost constant up to  $x = 0.48$  where it suddenly decreases. On the other hand, a monotonic increase is observed for bond length  $q$  and a monotonic reduction is found for bond angle  $\phi_l$  which moves away from  $180^\circ$ . The observed trend of  $q$  and  $\phi_l$  suggests a weakening of the A-O-B interaction with a subsequent reduction of ferrimagnetic alignment increasing the Zn content ( $x$ ).

### 3.2 Magnetic properties

Room temperature dc-magnetization loops of  $\text{Co}_{1-x}\text{Zn}_x\text{Fe}_2\text{O}_4$  powder samples taken at maximum magnetic field of 18 kOe are shown in Fig. 5; this behavior puts in evidence the variation of magnetic properties as a function of Zn content ( $x$ ). All curves exhibit a typical magnetic hysteretic loop indicating a ferromagnetic behavior at room temperature for all Zn concentrations. The evolution of coercive field ( $H_c$ ) as function of Zn content ( $x$ ) is shown in the inset of Fig. 5 and the values are reported in Table 3. The highest value of  $H_c$  is found at the highest  $\text{Co}^{2+}$  ions concentration ( $x = 0.08$ ) and it is due to the high anisotropy of  $\text{Co}^{2+}$  ions located at octahedral site resulting from its remarkable spin-orbit coupling. Increasing the Zn content ( $x$ ), a progressive decrease of  $H_c$  can be noted; this behavior can be reasonably attributed to the gradual reduction of magnetocrystalline anisotropy induced by lowering concentration of  $\text{Co}^{2+}$  ions at the octahedral site and also by a their partial migration from octahedral site to tetrahedral site (see Table 2).

Therefore, in this studied system, the substitution of non-zero angular momentum of ions ( $\text{Co}^{2+}$ ) with zero angular momentum ions ( $\text{Zn}^{2+}$ ) weakens the spin-orbit coupling and, consequently, the magnetocrystalline

anisotropy and the magnetic coercivity are reduced. Comparable behavior was found from different authors studying similar Co-Zn ferrites particles system [20,32,33,39]. On the other hand, the substitution of  $\text{Co}^{2+}$  ions with different ions such as Bi was found to induce a similar a decrease of the anisotropy, as expected, that however as a weaker effect on coercivity that turns out to be more affected by saturation magnetization than Co-Zn ferrite [40].

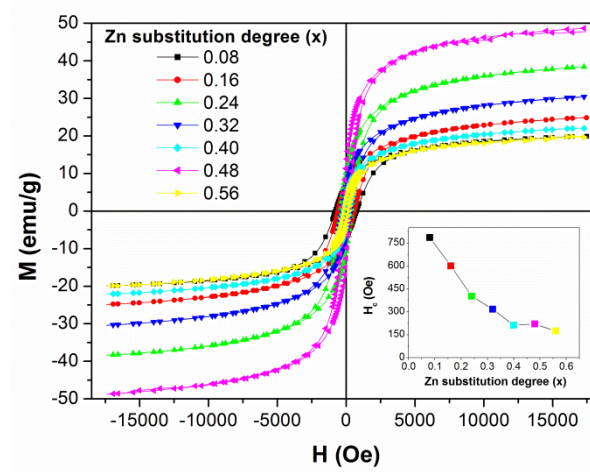


**Figure 5:** Room temperature dc-magnetization loops of  $\text{Co}_{1-x}\text{Zn}_x\text{Fe}_2\text{O}_4$  powder samples ( $0.08 < x < 0.56$ ); inset: evolution of coercive field as a function of Zn concentration.

The saturation magnetization at room temperature ( $M_s^{RT}$ ) of all samples is determined by fitting the high field region of magnetization curves with the expression  $M = M_s^{RT} - a/H$ , representing the first order approximation of series expansion that describes the law of approach to saturation [41]. The  $M_s^{RT}$  parameter (as well as  $a$ ) is set as free and the obtained values are reported in Table 3. The  $M_s^{RT}$  values depend on the Zn content (x) in a non-monotonous way that is mainly due to the non-equilibrium cation distribution in the samples. In addition it can be noted that the sample with the highest Co content ( $\text{Co}_{0.92}\text{Zn}_{0.08}\text{Fe}_2\text{O}_4$ ) shows a value of  $M_s^{RT}$  significantly lower than the bulk cobalt ferrite (80 emu/g [41]); this behavior can be attributed to the effect of a spin canting or a spin disorder at the surface of the ferrite crystals forming a magnetic dead layer that reduces the perfect alignment of spins and consequently the expected magnetization saturation value [42]. In addition, it is necessary to observe that the region of the hysteresis curve used to estimate the approach to saturation is close to the maximum applied field (18 kOe), that may not be sufficient to overcome the high anisotropy of the Co-based ferrite and to lead the samples to a complete saturation (see Fig.5). In this case, the

$M_s^{RT}$  values might be underestimated [40], however their trend with Zn content should be preserved (as confirmed by the comparison with  $M_s$  values at 2 K and 70 kOe, see table 3).

Nominal Zn content (x)	$H_c$ (Oe)	$M_s^{RT}$ (emu/g)	$M_r/M_s$ at T = 300 K	$M_s^{exp,2K}$ (emu/g)	$n_B^{calc}$	$\alpha_{YK}$ (°)	Static energy loss (J/kg) at $H_v = 18$ kOe
0.08	786	21.8	0.35	28.8	2.76	36.8	9.6
0.16	601	27.6	0.30	43.2	3.02	32.2	3.8
0.24	402	41.8	0.28	57.9	3.28	26.7	5.4
0.32	318	33.6	0.22	53.5	3.14	27.8	4.6
0.40	212	24.4	0.19	32.0	3.06	39.5	1.3
0.48	221	52.0	0.26	67.8	3.32	19.6	4.4
0.56	175	22.3	0.18	47.7	2.88	28.3	1.4

**Table 3.** Magnetic parameter as a function of nominal Zn content (x): coercive field ( $H_c$ ), saturation magnetization at room temperature ( $M_s^{RT}$ ), saturation magnetization at 2 K  $M_s^{2K}$ , calculated magnetic moment values ( $n_B^{calc}$ ), angle ( $\alpha_{YK}$ ) calculated by Yafet and Kittel model and static energy losses.

According to the Néel's two-sublattice model of ferrimagnets [43], the magnetic moments of the ions on the A and B sub-lattices are perfectly aligned anti-parallel to each other in a collinear structure in which any contribution of temperature is neglected; so the magnetic moment per formula unit ( $n_B^{calc}$ ) at T = 0 K can be calculated as:

$$n_B^{calc}(x) = M_B(x) - M_A(x) \quad (1)$$

where  $M_B$  and  $M_A$  are the magnetic moments in Bohr magnetons ( $\mu_B$ ) on B and A sub-lattices respectively. Therefore, using Eq. 1, the magnetic moment values ( $n_B^{calc}$ ) of all  $\text{Co}_{1-x}\text{Zn}_x\text{Fe}_2\text{O}_4$  powder samples have been calculated by taking the ionic magnetic moments of  $\text{Fe}^{3+} = 5 \mu_B$ ,  $\text{Co}^{2+} = 3 \mu_B$  and  $\text{Zn}^{2+} = 0 \mu_B$  [44] and by considering the cation distribution data reported in Table 2. The results of  $n_B^{calc}$  are in the range of 3.32 – 2.76  $\mu_B$  and are reported in Table 3.

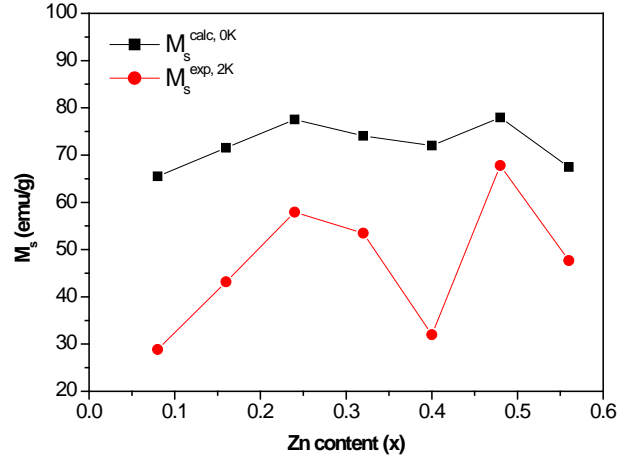


**Figure 6.** Comparison between calculated ( $M_s^{calc, 0K}$ , black squares) and experimental ( $M_s^{exp, 2K}$ , red dots) saturation magnetization as a function of Zn content (x).

In addition, the  $n_B^{calc}$  values can be converted to obtain the ferrite saturation magnetization ( $M_s^{calc, 0K}$ ) at  $T = 0$  K expressed in emu/g by means the expression proposed by Smit and Wijn [34]:

$$M_s^{calc, 0K}(x) = \frac{n_B^{calc}(x) \mu_B N_A}{M_w(x)} \quad (2)$$

where  $\mu_B$  is the Bohr Magneton,  $N_A$  is the Avogadro's number and  $M_w(x)$  is the molecular weight as function of Zn content (x). The evolution of  $M_s^{calc, 0K}(x)$  as function of Zn content (x) is shown in Fig. 6 where it is directly compared with the experimental values of ferrite saturation magnetization measured at  $T = 2$  K ( $M_s^{exp, 2K}$ ) by means of SQUID magnetometer. In this context, the comparison between the calculated and experimental saturation magnetization is performed assuming reasonably that  $M_s^{exp}(T = 2 \text{ K}) \approx M_s^{exp}(T = 0 \text{ K})$ . It is notable from this comparison that the experimental saturation magnetization values ( $M_s^{exp}(x)$ ) are systematically lower than those calculated by means of Neel's model ( $M_s^{calc}(x)$ ), but follow exactly the same trend and non-monotonous behavior.

This discrepancy between the experimental and calculated  $M_s$  values suggests that the magnetic arrangement of spins in our ferrite samples is not governed by a perfectly collinear antiparallel alignment, as proposed by Néel's model, but rather could be affected by a spin canting on the B site with respect to the

direction of spins on A site resulting in a non-collinear arrangement in the two-sublattices. This spin canting effect on all  $\text{Co}_{1-x}\text{Zn}_x\text{Fe}_2\text{O}_4$  powder samples can be explained by the three-lattice model suggested by Yafet and Kittel [45] and evaluated by calculating the Y-K angle ( $\alpha_{YK}$ ) by means of the following Eq. 3:

$$n_B^{exp,2K}(x) = M_B(x) \cos \alpha_{YK} - M_A(x) \quad (3)$$

where  $M_A(x)$  and  $M_B(x)$  are the magnetic moments expressed in Bohr magnetons ( $\mu_B$ ) on A and B sites, respectively, whereas  $n_B^{exp,2K}(x)$  is the experimental magnetic moment evaluated by inverting the equation (2) using the  $M_s^{exp,2K}$  values (see Table 3). The calculated  $\alpha_{YK}$  values, listed in Table 3, are in the range of  $19.6^\circ$  -  $36.8^\circ$  and are uncorrelated to Zn content (x); these high values of  $\alpha_{YK}$  suggest that the  $\text{Co}_{1-x}\text{Zn}_x\text{Fe}_2\text{O}_4$  ferrite samples are characterized by a strong spin canting effect that influences their magnetic properties.

In particular, Yafet – Kittel model suggests that the larger the  $\alpha_{YK}$  angle, the weaker is the A-O-B exchange interaction (responsible for ferrimagnetism) causing a reinforcement of B-O-B exchange interaction, inducing a consequent reduction of saturation magnetization as shown in Fig. 7. However, it is important to underline that this correlation between the  $\alpha_{YK}$  angle and the  $M_s^{exp,2K}$  values is also heavily affected by the Zn content (x) and the non-equilibrium cation distribution of studied samples (as mentioned above). As a consequence, the observed linear dependence of  $M_s^{exp,2K}$  on  $\alpha_{YK}$  is the result of multiple direct and indirect contributions acting both on microstructure and on magnetic interactions among the cations.

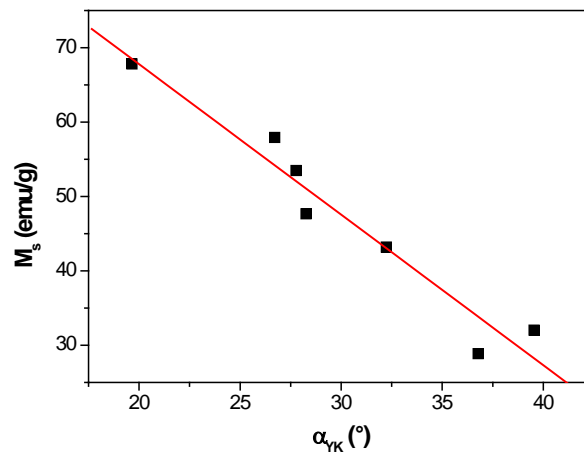


**Figure 7.** Correlation between experimental saturation magnetization  $M_s^{exp,2K}$  and Y-K angle ( $\alpha_{YK}$ ); the red line is a guide to the eye.

As mentioned before, other contributions that could add to the observed discrepancy between the experimental and calculated  $M_s$  values (see Fig. 6) are: 1) the low value of applied magnetic field around which the law of approach is used [40]; 2) the possible formation of a dead layer on ferrite surface arising from a spin disorder. As already observed by Kodama et al. [42] and El-Sayed et al. [46], this layer is formed due to the discontinuity of the magnetic interaction and the loss of long range order on the ferrite surface; consequently, it opposes the perfect alignment of the spins in the magnetic applied field direction and induces a reduction of saturation magnetization.

Although a deep understanding of the structure and the magnetic properties at the size scale of cations provides a fundamental step to practically use the ferrite in several fields, an evaluation of energy losses is also an important key point in the ferrite characterization since several applications involve the interaction between it and an external magnetic fields. In particular, the area enclosed by the dc-hysteresis curves (Fig. 5) represents the maximum energy lost by the samples along a major loop (applied a static field with vertex of 18 kOe); the measured values are shown in Table 3. The  $\text{Co}_{0.92}\text{Zn}_{0.08}\text{Fe}_2\text{O}_4$  sample characterized by the highest value of  $H_c$  ( $\approx 786$  Oe) shows also the highest value of energy losses ( $\approx 9.6$  J/kg) despite the lowest saturation magnetization value ( $\approx 21.8$  emu/g). In general, the energy loss value results to be a compromise between the enlargement of hysteresis loop due to the coercive field and the raising induced by the saturation magnetization.

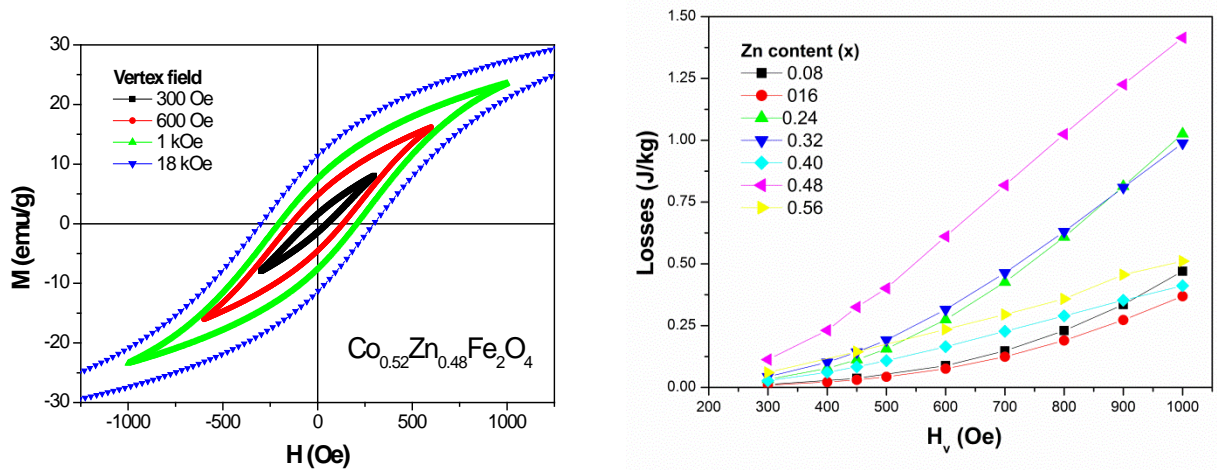


**Figure 8.** (a) Room temperature dc-hysteresis loop of  $\text{Co}_{0.52}\text{Zn}_{0.48}\text{Fe}_2\text{O}_4$  sample at selected vertex field; (b) static energy losses as function of vertex field.

Since the magnetic field amplitude involved in applications is usually not enough to saturate the ferrites magnetization, a study of energy losses evolution as a function of selected vertex field ( $H_v$ ) is performed in the



interval 300-1000 Oe in which the magnetization doesn't reach the complete saturation and describes minor loops. In this context, Fig. 8(a) shows a magnification of the major dc-hysteresis loop of the  $\text{Co}_{0.52}\text{Zn}_{0.48}\text{Fe}_2\text{O}_4$  sample and selected minor dc-hysteresis loops; whereas the energy loss values for all samples are displayed as a function of  $H_v$  in Fig. 8(b). In the studied vertex field range, the  $\text{Co}_{0.52}\text{Zn}_{0.48}\text{Fe}_2\text{O}_4$  sample displays the largest static energy losses for  $H_v$  up to 1 kOe (Fig. 8(b)). On the other hand, the sample with content of Zn  $x = 0.08$  shows very low energy losses in the investigated interval of  $H_v$  (Fig. 8(b)), conversely to  $H_v \approx 18$  kOe where it shows the highest values among studied samples (see Table 3).

In this context, it is worth mentioning that the static energy losses stem only from the magnetic anisotropy of the sample arising from its crystalline microstructure and/or local defects. The equilibrium condition employed to measure the static loops inhibits the formation of Eddy currents in the sample, therefore their contribution to the energy losses is not expected neither as dynamic losses (at the scale of the sample volume), nor as excess losses (at the scale of the domain walls or particles boundaries) [47]. For these reasons, the magnetic energy losses assessed from the area enclosed in static hysteresis loops are an underestimation with respect to the energy lost when the samples are used in high frequency applications, where the contribution of Eddy currents may not be negligible. However, the presented static measurements can nonetheless be useful and convenient tool in selecting the most promising ferrite materials also for high frequency applications in the suitable field range.

In order to evaluate the enhancement of energy losses at high frequency, dynamic hysteresis loops have been measured by a B-H loop tracer at a frequency of about 69 kHz. The magnetic field peak values ( $H_v$ ) of hysteresis loops are selected so that they are comparable to those exploited in static measurements, i.e. in the range 300 – 525 Oe. Fig. 9(a) shows dynamic hysteresis loops of  $\text{Co}_{0.52}\text{Zn}_{0.48}\text{Fe}_2\text{O}_4$ , and the observed behavior is representative of all other samples. Also in this case, the energy lost by each sample is evaluated by calculating the area enclosed in dynamic hysteresis loops at the selected  $H_v$ . Fig. 9(b) shows the dynamic hysteresis losses per unit mass for all studied ferrites as function of magnetic vertex field  $H_v$ . As expected, the dynamic energy losses turn out to be higher than the static ones (about 130 % in the  $\text{Co}_{0.52}\text{Zn}_{0.48}\text{Fe}_2\text{O}_4$  sample) because at 69 kHz the eddy currents are induced, prompting both dynamic and excess losses in the samples [47]. This increase is significant but not so huge because of the high electrical resistivity of sample hinders the flow of Eddy current.

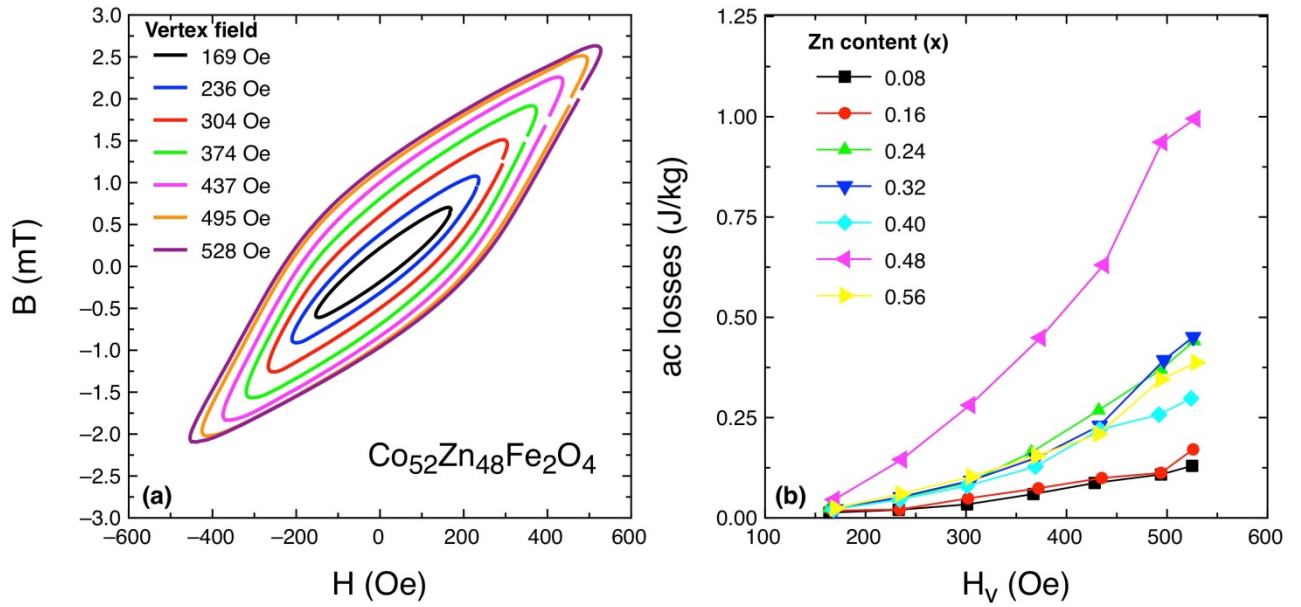


**Figure 9.** (a) Room temperature ac-hysteresis loop of  $\text{Co}_{0.52}\text{Zn}_{0.48}\text{Fe}_2\text{O}_4$  sample at selected vertex field; (b) dynamic energy losses as function of vertex field.

## 4. Conclusion

Zn-substituted  $\text{CoFe}_2\text{O}_4$  powder samples with different Zn content have been prepared by a sol gel auto-combustion method at low temperature ( $< 110^\circ\text{C}$ ). The lack of a post-synthesis heat treatment represents an advantage for the industrial synthesis process. However, it has a strong influence on the magnetic properties leading to a non-equilibrium cation distribution in the nanocrystalline mixed cubic spinel structure immediately reflected on measured  $M_s$  behavior. The gas release during the synthesis process induces a micrometric agglomerate morphology of powders containing nanocrystallites in the size range between 23 – 35 nm. The cation distribution is obtained analyzing the XRD data via the Bartaut method. The sample with the lowest  $\text{Zn}^{2+}$  content ( $x = 0.08$ ) results with a completely inverse spinel structure ( $\delta = 0$ ), whereas  $\delta$  increases with increasing  $\text{Zn}^{2+}$  content ending up to a totally random distribution ( $\delta = 0.33$ ) for  $x = 0.56$ . Moreover, the lattice parameter and the oxygen position are affected by the substitution of the smaller  $\text{Co}^{2+}$  ions with the larger  $\text{Zn}^{2+}$  ions.

The magnetic properties are strongly affected by the sample composition and by the cation distribution within the ferrite structure. In particular, the replacement of non-zero angular momentum  $\text{Co}^{2+}$  ions with zero angular momentum  $\text{Zn}^{2+}$  ions induces a reduction of magnetocrystalline anisotropy reflected in the coercive field values; whereas the mutual distribution of  $\text{Co}^{2+}$  ions ( $3 \mu_B$ ) and  $\text{Zn}^{2+}$  ( $0 \mu_B$ ) in the sub-lattices intensely affects the saturation magnetization following the Yafet-Kittel's model.

The energy losses evaluated by the dc-hysteresis loops taken at selected vertex field results to be a under-estimation with respect to the energy losses when the samples are submitted to ac-magnetic field of the same field values, however, this procedure can be a useful and convenient tool in selecting the most promising ferrite materials for high frequency applications in the suitable field range.

## Competing interests

The authors have no competing interests to declare

## Funding

This research did not receive any specific grant from funding agencies in the public, commercial, or not-for-profit sectors.

## References

- [1] I.H. Gul, A. Maqsood, Structural, magnetic and electrical properties of cobalt ferrites prepared by the sol-gel route, *J. Alloys Compd.* 465 (2008) 227–231. doi:10.1016/j.jallcom.2007.11.006.
- [2] G.L. Sun, J.B. Li, J.J. Sun, X.Z. Yang, The influences of  $\text{Zn}^{2+}$  and some rare-earth ions on the magnetic properties of nickel-zinc ferrites, *J. Magn. Magn. Mater.* 281 (2004) 173–177. doi:10.1016/j.jmmm.2004.04.099.
- [3] R. V. Mangalaraja, S. Ananthakumar, P. Manohar, F.D. Gnanam, Magnetic, electrical and dielectric behaviour of  $\text{Ni}_{0.8}\text{Zn}_{0.2}\text{Fe}_2\text{O}_4$  prepared through flash combustion technique, *J. Magn. Magn. Mater.* 255 (2002) 56–64. doi:10.1016/S0304-8853(02)00413-4.
- [4] J.F. Hocheplied, M.P. Pileni, Magnetic properties of mixed cobalt–zinc ferrite nanoparticles, *J. Appl. Phys.* 87 (2000) 2472–2478. doi:10.1063/1.372205.
- [5] A. López-Ortega, E. Lottini, C.D.J. Fernández, C. Sangregorio, Exploring the Magnetic Properties of

Cobalt-Ferrite Nanoparticles for the Development of a Rare-Earth-Free Permanent Magnet, *Chem. Mater.* 27 (2015) 4048–4056. doi:10.1021/acs.chemmater.5b01034.

- [6] H. Montiel, G. Alvarez, M.P. Gutiérrez, R. Zamorano, R. Valenzuela, Microwave absorption in Ni-Zn ferrites through the Curie transition, *J. Alloys Compd.* 369 (2004) 141–143. doi:10.1016/j.jallcom.2003.09.074.
- [7] K. Khan, Microwave absorption properties of radar absorbing nanosized cobalt ferrites for high frequency applications, *J. Supercond. Nov. Magn.* 27 (2014) 453–461. doi:10.1007/s10948-013-2283-4.
- [8] A.N. Yusoff, M.H. Abdullah, Microwave electromagnetic and absorption properties of some LiZn ferrites, *J. Magn. Magn. Mater.* 269 (2004) 271–280. doi:10.1016/S0304-8853(03)00617-6.
- [9] D.S. Mathew, R.S. Juang, An overview of the structure and magnetism of spinel ferrite nanoparticles and their synthesis in microemulsions, *Chem. Eng. J.* 129 (2007) 51–65. doi:10.1016/j.cej.2006.11.001.
- [10] L. Gastaldi, A. Lapicciarella, Three Different Methods Spinel : A Comparison of Determining the Cation Distribution in, (1979).
- [11] D. Peddis, N. Yaacoub, M. Ferretti, A. Martinelli, G. Piccaluga, A. Musinu, C. Cannas, G. Navarra, J.M. Greneche, D. Fiorani, Cationic distribution and spin canting in  $\text{CoFe}_2\text{O}_4$  nanoparticles, *J. Phys. Condens. Matter.* 23 (2011) 426004. doi:10.1088/0953-8984/23/42/426004.
- [12] V.G. Harris, N.C. Koon, C.M. Williams, Q. Zhang, M. Abe, J.P. Kirkland, Cation distribution in NiZn-ferrite films via extended x-ray absorption fine structure, *Appl. Phys. Lett.* 68 (1996) 2082–2084. doi:10.1063/1.115591.
- [13] S.P. Yadav, S.S. Shinde, P. Bhatt, S.S. Meena, K.Y. Rajpure, Distribution of cations in  $\text{Co}_{1-x}\text{Mn}_x\text{Fe}_2\text{O}_4$  using XRD, magnetization and Mössbauer spectroscopy, *J. Alloys Compd.* 646 (2015) 550–556. doi:10.1016/j.jallcom.2015.05.270.
- [14] D. V. Kurmude, R.S. Barkule, a. V. Raut, D.R. Shengule, K.M. Jadhav, X-Ray Diffraction and Cation Distribution Studies in Zinc-Substituted Nickel Ferrite Nanoparticles, *J. Supercond. Nov. Magn.* 27 (2013) 547–553. doi:10.1007/s10948-013-2305-2.
- [15] A. Najafi Birgani, M. Niyafar, A. Hasanpour, Study of cation distribution of spinel zinc nano-ferrite

by X-ray, *J. Magn. Magn. Mater.* 374 (2015) 179–181. doi:10.1016/j.jmmm.2014.07.066.

- [16] V. Šepelák, L. Wilde, U. Steinike, K.D. Becker, Thermal stability of the non-equilibrium cation distribution in nanocrystalline high-energy milled spinel ferrite, *Mater. Sci. Eng. A.* 375–377 (2004) 865–868. doi:10.1016/j.msea.2003.10.179.
- [17] V. Šepelák, I. Bergmann, A. Feldhoff, P. Heitjans, F. Krumeich, D. Menzel, F.J. Litterst, S.J. Campbell, K.D. Becker, Nanocrystalline nickel ferrite,  $\text{NiFe}_2\text{O}_4$ : Mechanosynthesis, nonequilibrium cation distribution, canted spin arrangement, and magnetic behavior, *J. Phys. Chem. C.* 111 (2007) 5026–5033. doi:10.1021/jp067620s.
- [18] V. Šepelák, S.M. Becker, I. Bergmann, S. Indris, M. Scheuermann, A. Feldhoff, C. Kübel, M. Bruns, N. Stürzl, A.S. Ulrich, M. Ghafari, H. Hahn, C.P. Grey, K.D. Becker, P. Heitjans, Nonequilibrium structure of  $\text{Zn}_2\text{SnO}_4$  spinel nanoparticles, *J. Mater. Chem.* 22 (2012) 3117. doi:10.1039/c2jm15427g.
- [19] R. Arulmurugan, B. Jeyadevan, G. Vaidyanathan, S. Sendhilnathan, Effect of zinc substitution on Co-Zn and Mn-Zn ferrite nanoparticles prepared by co-precipitation, *J. Magn. Magn. Mater.* 288 (2005) 470–477. doi:10.1016/j.jmmm.2004.09.138.
- [20] R. Arulmurugan, G. Vaidyanathan, S. Sendhilnathan, B. Jeyadevan, Co-Zn ferrite nanoparticles for ferrofluid preparation: Study on magnetic properties, *Phys. B Condens. Matter.* 363 (2005) 225–231. doi:10.1016/j.physb.2005.03.025.
- [21] G.A. Sawatzky, F. Van Der Woude, A.H. Morrish, Cation distributions in octahedral and tetrahedral sites of the ferrimagnetic spinel  $\text{CoFe}_2\text{O}_4$ , *J. Appl. Phys.* 39 (1968) 1204–1205. doi:10.1063/1.1656224.
- [22] M. Veverka, Z. Jiráček, O. Kaman, K. Knížek, M. Maryško, E. Pollert, K. Závěta, A. Lančok, M. Dlouhá, S. Vratislav, Distribution of cations in nanosize and bulk Co-Zn ferrites, *Nanotechnology.* 22 (2011) 345701. doi:10.1088/0957-4484/22/34/345701.
- [23] M. Satalkar, S.N. Kane, A. Ghosh, N. Ghodke, G. Barrera, F. Celegato, M. Coisson, P. Tiberto, F. Vinai, Synthesis and soft magnetic properties of  $\text{Zn}_{0.8-x}\text{Ni}_x\text{Mg}_{0.1}\text{Cu}_{0.1}\text{Fe}_2\text{O}_4$  ( $x = 0.0-0.8$ ) ferrites prepared by sol-gel auto-combustion method, *J. Alloys Compd.* 615 (2015) S313–S316. doi:10.1016/j.jallcom.2014.01.248.
- [24] S.T. Aruna, A.S. Mukasyan, Combustion synthesis and nanomaterials, *Curr. Opin. Solid State Mater.*

Sci. 12 (2008) 44–50. doi:10.1016/j.cossms.2008.12.002.

- [25] F. Bertaut, Etude de la nature des ferrites spinelles, *Comptes Rendus Hebd. Des Seances L'Academie Des Sci.* 230 (1950) 213–215.
- [26] M. Coisson, G. Barrera, F. Celegato, L. Martino, S.N. Kane, S. Raghuvanshi, F. Vinai, P. Tiberto, Hysteresis losses and specific absorption rate measurements in magnetic nanoparticles for hyperthermia applications, *Biochim. Biophys. Acta - Gen. Subj.* 1861 (2017) 1545–1558. doi:10.1016/j.bbagen.2016.12.006.
- [27] L. Lutterotti, P. Scardi, Simultaneous structure and size–strain refinement by the Rietveld method, *J. Appl. Crystallogr.* 23 (1990) 246–252. doi:10.1107/S0021889890002382.
- [28] L. Yu, S. Cao, Y. Liu, J. Wang, C. Jing, J. Zhang, Thermal and structural analysis on the nanocrystalline NiCuZn ferrite synthesis in different atmospheres, *J. Magn. Mater.* 301 (2006) 100–106. doi:10.1016/j.jmmm.2005.06.020.
- [29] A.C.F.M. Costa, V.J. Silva, C.C. Xin, D.A. Vieira, D.R. Cornejo, R.H.G.A. Kiminami, Effect of urea and glycine fuels on the combustion reaction synthesis of Mn-Zn ferrites: Evaluation of morphology and magnetic properties, *J. Alloys Compd.* 495 (2010) 503–505. doi:10.1016/j.jallcom.2009.10.065.
- [30] A. Sutka, G. Mezinskas, Sol-gel auto-combustion synthesis of spinel-type ferrite nanomaterials, *Front. Mater. Sci.* 6 (2012) 128–141. doi:10.1007/s11706-012-0167-3.
- [31] M. Lakshmi, K.V. Kumar, K. Thyagarajan, Structural and Magnetic Properties of Cr-Co Nanoferrite Particles, (2016) 103–113.
- [32] G. Vaidyanathan, S. Sendhilnathan, Characterization of  $\text{Co}_{1-x}\text{Zn}_x\text{Fe}_2\text{O}_4$  nanoparticles synthesized by co-precipitation method, *Phys. B Condens. Matter.* 403 (2008) 2157–2167. doi:10.1016/j.physb.2007.08.219.
- [33] I. Sharifi, H. Shokrollahi, Nanostructural, magnetic and Mössbauer studies of nanosized  $\text{Co}_{1-x}\text{Zn}_x\text{Fe}_2\text{O}_4$  synthesized by co-precipitation, *J. Magn. Mater.* 324 (2012) 2397–2403. doi:10.1016/j.jmmm.2012.03.008.
- [34] J. Smit, H.P.J. Wijn, Ferrites, (1959) 384.
- [35] M.R. De Guire, R.C. O’Handley, G. Kalonji, The cooling rate dependence of cation distributions in  $\text{CoFe}_2\text{O}_4$ , *J. Appl. Phys.* 65 (1989) 3167–3172. doi:10.1063/1.342667.

- [36] C.K. Kim, J.H. Lee, S. Katoh, R. Murakami, M. Yoshimura, Synthesis of Co-, Co-Zn and Ni-Zn ferrite powders by the microwave-hydrothermal method, *Mater. Res. Bull.* 36 (2001) 2241–2250. doi:10.1016/S0025-5408(01)00703-6.
- [37] A.R. Denton, N.W. Ashcroft, Vegard's law, *Phys. Rev. A* 43 (1991) 3161–3164.
- [38] G. Kumar, J. Shah, R.K. Kotnala, V.P. Singh, Sarveena, G. Garg, S.E. Shirsath, K.M. Batoo, M. Singh, Superparamagnetic behaviour and evidence of weakening in super-exchange interactions with the substitution of  $Gd^{3+}$  ions in the Mg-Mn nanoferrite matrix, *Mater. Res. Bull.* 63 (2015) 216–225. doi:10.1016/j.materresbull.2014.12.009.
- [39] V. Mameli, A. Musinu, A. Ardu, G. Ennas, D. Peddis, D. Niznansky, C. Sangregorio, C. Innocenti, N.T.K. Thanh, C. Cannas, Studying the effect of Zn-substitution on the magnetic and hyperthermic properties of cobalt ferrite nanoparticles, *Nanoscale*. 8 (2016) 10124–10137. doi:10.1039/C6NR01303A.
- [40] A. Franco, F.L.A. MacHado, V.S. Zapf, F. Wolff-Fabris, Enhanced magnetic properties of Bi-substituted cobalt ferrites, *J. Appl. Phys.* 109 (2011) 10–14. doi:10.1063/1.3565406.
- [41] B.D. Cullity, C.D. Graham, *Introduction to Magnetic Materials*, 2009.
- [42] R.H. Kodama, a E. Berkowitz, E.J. McNiff Jr., S. Foner, Surface Spin Disorder in  $NiFe_2O_4$  Nanoparticles, *Phys. Rev. Lett.* 77 (1996) 394–397. doi:10.1103/PhysRevLett.77.394.
- [43] A. Fairweather, F.F. Roberts, A.J.E. Welch, Ferrites, *Reports Prog. Phys.* 15 (1952) 306. doi:10.1088/0034-4885/15/1/306.
- [44] J.M.D. Coey, *Magnetism and Magnetic Materials*, 2009.
- [45] N.S.S. Murthy, M.G. Natera, S.I. Youssef, R.J. Begum, C.M. Srivastava, Yafet-kittel angles in zinc-nickel ferrites, *Phys. Rev.* 181 (1969) 969–977. doi:10.1103/PhysRev.181.969.
- [46] H.M. El-Sayed, I.A. Ali, A. Azzam, A.A. Sattara, Influence of the magnetic dead layer thickness of Mg-Zn ferrites nanoparticle on their magnetic properties, 424 (2017) 226–232.
- [47] G. Bertotti, *Hysteresis in Magnetism: For Physicists, Materials Scientists, and Engineers*, Academic Press, 1998.

